Available online at www.sciencedirect.com

SciVerse ScienceDirect

journal homepage: www.elsevier.com/locate/he

ELSEVIER

Chemical and transport behaviors in a microfluidic reformer with catalytic-support membrane for efficient hydrogen production and purification

Jin Xuan [a], Dennis Y.C. Leung [a,], Michael K.H. Leung [b], Meng Ni [c], Huizhi Wang [a]*

[a] *Department of Mechanical Engineering, The University of Hong Kong, Hong Kong, China*
[b] *Ability R&D Energy Research Centre, School of Energy and Environment, City University of Hong Kong, Hong Kong, China*
[c] *Department of Building and Real Estate, Hong Kong Polytechnic University, Hong Kong, China*

ARTICLE INFO

ABSTRACT

Microchannel reformer integrated with H_2 selective membrane offers an efficient, compact and portable way to produce hydrogen. The performance of a membrane-based microfluidic reformer is restricted by species diffusion limitation within the porous support of the membrane. Recent development in novel catalytic-supported membranes has the potential to enhance H_2 production by decimating the diffusion limitation. Loading a Pd-Ag layer on to a Ni-catalytic porous support, the membrane achieves both H_2 separation and production functions. In this study, a two-dimensional CFD model combined with chemical kinetics has been developed to simulate a microchannel autothermal reformer fed by methane. The species conversion and transport behaviors have been studied. The results show that the permeation process enhances the mass transport within the catalytic layer, and as a result, the reactions are intensified. Most notably, the effectiveness factor of the water-gas shift reaction as high as 6 is obtained. In addition, the effects of gaseous hourly space velocity (GHSV) on methane conversion and H_2 flux through the membrane are also discussed, and an optimal value of GHSV is suggested.

1. Introduction

The microfabrication technologies and micro-scale devices have been introduced in reforming hydrocarbon fuel for hydrogen production, to meet the increasing demand of developing portable fuel-cell based power sources [1–4]. Micro-scale reformers have shown capabilities considerably exceeding of macroscale systems such as packed-beds [1]. Among various types of micro-reformers, the microchannel reformer has received most interests as it can provide extremely high surface-to-volume ratio, efficient mass and heat transfer, and low flow resistance.

Integration of H_2 separation membrane in microchannel reformers has been studied to purify H_2 and intensify the reactions [2]. Conventional membrane consists of a thin functional layer (typically Pd-based alloy layer or silica-based layer) to separate hydrogen and a porous support to provide mechanical strength. One challenge associated with the design is the high resistance of the hydrogen flux through the thick membrane. With the development of fabrication

Nomenclature

A_{cell}	area of computational cell, m^2
C	inertial loss coefficient, m^{-1}
C_p	specific heat, $J\,kg^{-1}\,K^{-1}$
D_{pore}	mean diameter of the pore, m
D_i^p	diffusion coefficient in the porous media of species i, $m^2\,s^{-1}$
$D_{i,m}$	diffusion coefficient in the mixture of species i, $m^2\,s^{-1}$
$D_{i,j}$	binary mass diffusion coefficient of species i, $m^2\,s^{-1}$
d^m	membrane thickness, m
F	Forchheimer coefficient
h_i	enthalpy of species i, $J\,kg^{-1}$
J_{H2}^{Mem}	permeation rate of H_2 through the membrane, $mol\,m^{-2}\,s^{-1}$
M_i	molecular weight of species i, $kg\,kmol^{-1}$
k_f	fluid phase thermal conductivity, $W\,m^{-1}\,K^{-1}$
k_s	solid phase thermal conductivity, $W\,m^{-1}\,K^{-1}$
R	universal constant, $kJ\,kmol^{-1}\,K^{-1}$
R_i	ith reaction rate, $kmol\,m^{-3}\,s^{-1}$
r_i	reaction rate of species , $kmol\,m^{-3}\,s^{-1}$
p_i	partial pressure of species i, bar
p	pressure, Pa

Q^m	membrane permeance, $mol\,m^{-1}\,s^{-1}\,Pa^{-n}$
Q_s	energy supply for heating, $j\,kg^{-1}$
S	source term
T	temperature, K
U	superficial velocity, $m\,s^{-1}$
V_{cell}	volume of computational cell, m^3
X_i	mole fraction of species i
Y_i	mass fraction of species i

Greek letters

γ	porosity
ρ	density, $kg\,m^{-3}$
$\bar{\bar{\tau}}$	stress tensor, Pa
τ	torsity
μ	viscosity, Pa s
η	effectiveness factor
κ	permeability, m^2

Subscripts

s	solid phase
f	fluid phase
pm	porous media

Superscripts

P	permeation side
R	reforming side

technology, the separating layer can be split from its porous support with the membrane thickness reduced below 5 μm, which is known as self-support membrane [5]. More recently, a new concept of catalytic-support membrane has been reported [2,6,7]. In a catalytic-support membrane, the catalytic porous support (e.g. Ni/Al₂O₃) is used instead of conventional non-reactive support. It combines both catalytic activity and separation ability into one membrane rather than one reactor. The chemical and transport patterns for the three above-mentioned types of membrane applying to a microchannel reformer are summarized in Fig. 1. It can be found that the reformer using catalytic-support membrane subjects to the shortest conversion and transport path, and correspondingly lowest resistance. The design has been demonstrated capable of breaking the performance restrains related to mass transfer limitation, such as concentration polarizations and hydrogen dilution [2,6].

Some researches on the fabrication and utilization of the catalytic-support membrane have been reported [1,2,6,7]. However, it is difficult to directly measure the local physi-ochemical interactions and micro-scale transport behaviors in the porous membrane using conventional experimental techniques, resulting in a lack of in-depth understanding on the underlay processes and sufficient knowledge to optimize the system. This paper employs a computational fluid dynamics (CFD) model integrated with chemical kinetics to simulate the process of hydrogen production and purification in a microfluidic reformer. The chemical and transport behaviors within the catalytic-support membrane will be emphasized with an aim to provide theoretical implications for further development and optimization of the design.

2. Methodology

2.1. Physical model and computational domain

In this work, we conceptually considered a membrane microchannel reformer based on readily available fabrication and assembling technologies [1,2,6,7]. The reformer can be designed to have multiple microchannel pairs with a catalytic-supported membrane arranged in parallel. Auto-thermal reforming (ATR) of CH₄ is chosen as the reaction, which will take place at the catalytic-support layer located in the reactive channel. For the membrane, the hydrogen selective permeation can be achieved by silica layer [6,7] or Pd-based metallic layer [2]. Here, the separating layer of the catalytic-support membrane is assumed to be a Pd–Ag layer due to its well-established permeation rate expression to facilitate the computation. In the reformer, the H₂ produced will instantaneously permeate through the Pd–Ag layer of the membrane to the permeation channel. Sweep gas is used to sufficiently remove the permeated H₂. Since the main interests of this study are the local heat and mass transfer phenomena rather than the whole system performance, a representative channel-pair unit extracted from the reformer has been selected for detailed analysis. A two-dimensional computational domain is built based on the physical model, as shown in Fig. 2. The inlet and outlet are set far enough from the reaction region, to prevent any influence from them on the model results. Structured grids are used in the domain with grid independence ensured in each simulation case.
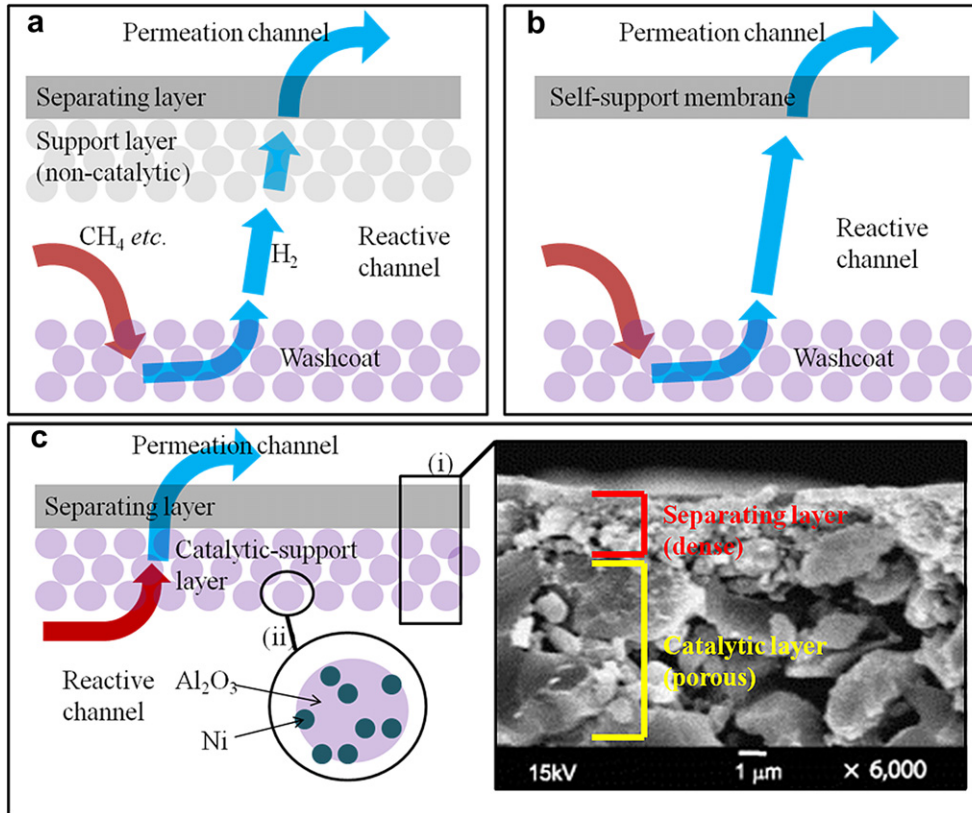
Fig. 1 – Chemical and reaction patterns in fuel reformer with (a) conventional membrane; (b) self-support membrane; and (c) catalytic-support membrane (the cross-sectional SEM image of catalytic-support membrane is reprinted from [5]).

2.2. *Flow characterization and properties determination*

As the simulation is conducted under microfluidic scale, it is important to characterize the flow and check any possible scale effects that may affect the validity of the CFD model based on continuum assumption [8]. Taking into account the approximated range of operating conditions, geometric parameters, and fluid properties for channels and catalytic layer, the Knudsen numbers in gas channels (Kn_{gas}) are estimated to be $\sim 10^{-3}$, which is lower than the threshold of 10^{-2}, indicating that consideration of the rarefied gas effect is not necessary [8].

Diffusivity is an important flow property considered in this model and it is governed by different regimes. Since the local Kn number in the catalytic porous layer (Kn_{porous}) is of the magnitude of 10^3, the diffusion in its pores is dominated by Knudsen diffusion. The ordinary (Fickian) diffusion, which only becomes significant when $Kn < 10$, can be omitted [8]. The effective diffusion coefficient of species i in the catalytic layer can be determined by kinetic theory and parallel pore model [8]:

$$D_i^p = \frac{\gamma}{\tau} 43.5 d_{pore} \left(\frac{T}{M_i} \right)^{0.5}. \tag{1}$$

Contrarily, the ordinary diffusion regime is found in the two microchannels. The Fickian diffusion (dilute approximation) model has been demonstrated to have nearly equivalent accuracy with Stefan–Maxwell model in the situation similar
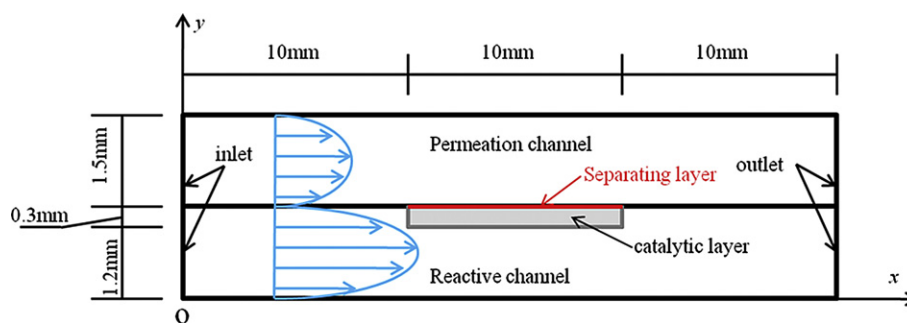

Fig. 2 – Illustration of the computational domain and the hydrodynamic conditions (not in scale).

with this study [9]. Therefore, it is chosen to calculate the diffusion coefficient in the two microchannels:

$$D_{i,m}^c = \frac{1 - X_i}{\sum_{j,j \neq i} \left(\frac{X_j}{D_{i,j}} \right)}. \tag{2}$$

The binary mass diffusion coefficients, $D_{i,j}$, are calculated by Chapman—Enskog formula using kinetic theory [10].

In this study, the fluid is treated as a multi-component ideal gas, and its composition-dependent density is calculated as:

$$\rho = \frac{p}{RT \sum_i \frac{Y_i}{M_i}}. \tag{3}$$

Since the pressure drops along the channels are small enough (in magnitude of 10^{-1} Pa) to be omitted, constant values of absolute pressure are adopted in the above equation, i.e. $p = 1$ atm at the permeation channel, and $p = p_{op}$ at the reactive channel.

2.3. Microchannel

Neglecting the rarefied gas effects, the behaviors of multi-component flow in microchannels are mathematically described by the well-known group of continuity equation, Navier—Stokes equation, energy equation, and species transport equations [10]. Since the above-mentioned equations are widely documented in literatures [11—15], they will not be individually listed here. In particular, source terms are added to the continuity equation to account for the mass of permeated hydrogen in the computational cells adjunct to the separating layer:

$$\nabla \cdot (\rho U) = S_{mass}; \tag{4}$$

The source terms S_{mass} is related to membrane permeation rate and their expressions will be given in Section 2.5.

2.4. Catalytic-support layer

In the catalytic-support layer, continuity equation (Eq. (4)) is still applicable, while the Darcy—Brinkman—Forchheimer equation is used instead of the standard Navier—Stokes equation to describe the non-Darcian behavior of the flow in the porous catalytic layer:

$$\nabla \cdot (\rho UU) = -\nabla p + \nabla \cdot \bar{\bar{\tau}} - \frac{\mu}{\kappa} U - \frac{F \gamma}{\sqrt{\kappa}} \rho U^2. \tag{5}$$

This equation takes account of the interactions between the porous and clear flow, and is widely used to solve the paralleled porous-clear streams with high accuracy [16]. Flow changes due to reaction are also considered in the coupled manner by solving local pressure, viscosity and density.

In another aspect, the heat and mass transfer is also affected by the porous structure. These effects are considered together with source terms contributed by chemical reactions and membrane permeation, which result in the derivation of the following energy and species transport equations.
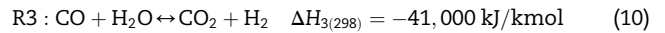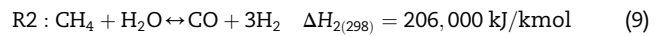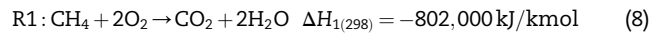
$$\left((\rho C_p)_s (1 - \gamma) + (\rho C_p)_f \gamma \right) \cdot U \cdot \nabla T_{pm}$$
$$= \nabla \cdot \left[(\gamma k_f + (1 - \gamma) k_s) \nabla T_{pm} \right] - \sum_i \frac{h_i^0}{M_i} r_i; \tag{6}$$

$$\nabla \cdot (\rho U Y_i) = \nabla \cdot (\rho D_i^p \nabla Y_i) + S_i + M_i r_i. \tag{7}$$

The last terms on the RHS of the above two reactions (6) and (7) are the source terms to account for the local heat generated by chemical reactions and consumption/generation of species, respectively.

2.5. Chemical kinetics and membrane permeation rate

The autothermal reforming of methane can be described by the following four sub-reactions.

$$R1: CH_4 + 2O_2 \rightarrow CO_2 + 2H_2O \quad \Delta H_{1(298)} = -802,000 \, kJ/kmol \tag{8}$$

$$R2: CH_4 + H_2O \leftrightarrow CO + 3H_2 \quad \Delta H_{2(298)} = 206,000 \, kJ/kmol \tag{9}$$

$$R3: CO + H_2O \leftrightarrow CO_2 + H_2 \quad \Delta H_{3(298)} = -41,000 \, kJ/kmol \tag{10}$$

$$R4: CH_4 + 2H_2O \leftrightarrow CO_2 + 4H_2 \quad \Delta H_{4(298)} = 165,000 \, kJ/kmol \tag{11}$$

R1 is complete oxidation of CH_4; R2 and R4 are steam reforming of CH_4; and R3 is water-gas shift reaction. The above four reaction system can automatically reach a thermal balance, if the mole ratio of species in the feedstock is proper. Therefore, it is named as autothermal reforming, which is a common reaction route for hydrogen production. One of the well-established kinetics schemes for the above reactions on Ni catalyst was originally reported by Xu and Froment [17], and Ma et al. [18], and then extensively adopted by other researchers [19—21]. In this study, we also use this kinetics scheme, of which detailed expression is available elsewhere [19]. Note that this study deals with intrinsic kinetics. As a result, the effectiveness factor (an important input parameter for macroscopic reactor models to adjust the kinetics expressions to account for the effect of internal diffusion) [17] of each sub-reaction is not necessarily to be assumed. On the contrary, it is one of the expected outputs from the model results.

The H_2 permeation process through the Pd—Ag membrane is governed by a solution—diffusion mechanism, where the gas molecules are dissolved in the membrane surface at the high partial pressure side and desorbed at the low partial pressure side. In this study, the power law equations are adopted to predict the permeation rate:

$$J_{H_2}^{Mem} = \frac{Q_{H_2}^m}{d_{H_2}^m} \exp \left(-\frac{E_{H_2}^m}{RT} \right) \left[\left(p_{H_2,M}^R \right)^n - \left(p_{H_2,M}^P \right)^n \right]. \tag{12}$$

The kinetics parameters involved can be referred to [22], and particularly, the thickness of the membrane in this study is set to be 3 μm.

Special source terms are applied to the continuity and species transport equations in the computational cell adjunct to both sides of the separating layer, in order to couple the above two equations to the volumetric-based CFD solver [23—25]:

$$S_{mass} = S_{H_2} = \begin{cases} \dfrac{J_{H_2}^{Mem} \cdot A_{cell}}{V_{cell}} \text{ at higher } H_2 \text{ partial pressure side} \\ -\dfrac{J_{H_2}^{Mem} \cdot A_{cell}}{V_{cell}} \text{ at lower } H_2 \text{ partial pressure side} \end{cases} \quad (13)$$

At the other computational cells, the source terms remain 0. The boundary conditions of the governing equations are considered as:

$$\text{at walls}: \ U = \frac{\partial Y_i}{\partial y} = \nabla T = 0; \quad (14)$$

$$\text{at flow inlet}: \ m = m_{in}; \quad (15)$$

$$\text{at flow outlet}: \ \nabla U = \nabla Y_i = \nabla T = 0; \quad (16)$$

at membrane and separating wall between two channels :

$$U = \frac{\partial Y_i}{\partial y} = 0. \quad (17)$$

2.6. Numerical procedures

The general-purpose CFD code FLUENT 6.3 [10] based on finite volume method was utilized in this study for the numerical procedure. The chemical kinetics model and membrane permeation model are coupled with the CFD by User-Defined Function (UDF). For each iteration, the chemical reaction and membrane permeation rates are calculated with local species mass fraction, temperature and density of respective computational cell in the reactive zone.
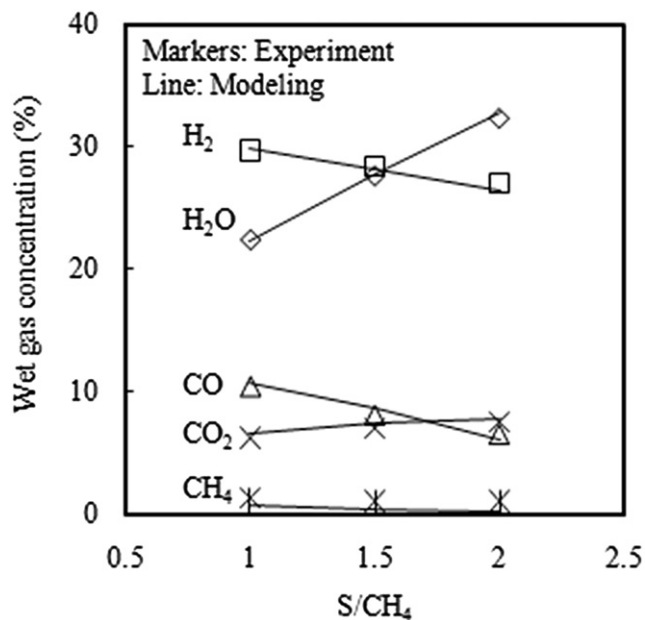

Fig. 3 – Comparison between predicted and measured [26] gas concentrations at different S/CH₄ ratios in an ATR reformer.
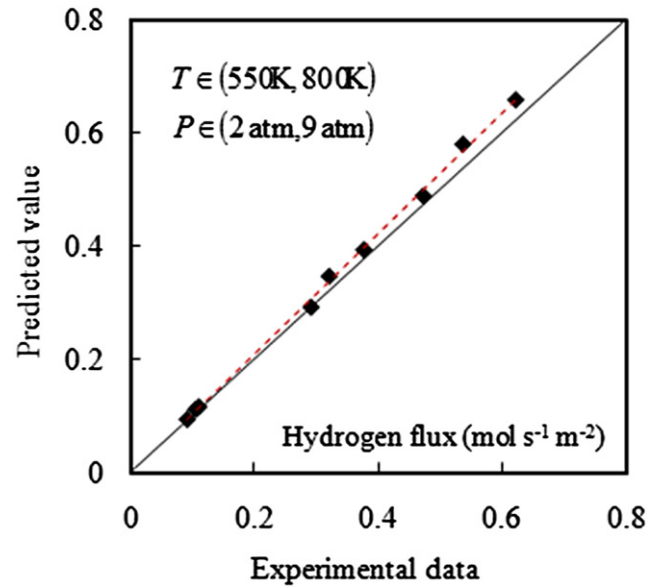

Fig. 4 – Comparison between predicted and measured [27] hydrogen permeation flux at different operating conditions in a permeation cell.

3. Results and discussion

3.1. Model validation

Since there is a lack of experimental data for a direct comparison with our model results, the ATR coupled CFD model and H_2 permeation coupled CFD model are validated separately. While detailed model validation can be found in our previous work [23], a brief description is provided here. The ATR model is compared with the experimental study on autothermal reforming of methane in a packed-bed reformer [26] as shown in Fig. 3. It is found that the agreement is reasonably good. The H_2 permeation model is compared with the experimental study on a H_2 permeation cell by Yang et al. [27]. The comparison between predicted and measured H_2 flux through the membrane is shown in Fig. 4. Acceptable accuracy can also be found. It suggests that the model framework can predict various physicochemical interactions in a reactor including autothermal reforming, hydrogen permeation, gas transport in a microchannel and reactant transport and reaction in porous media, all of which are major elements in the present microfluidic catalytic-support membrane reformer.

Table 1 – Simulation conditions of the studied catalytic-support membrane microchannels.

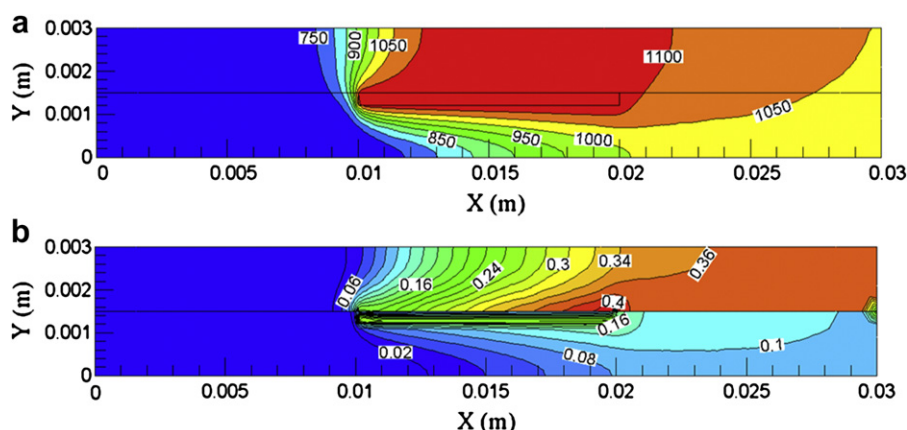| Parameters	Values
Reactive channel inlet velocity	0.18 m s^{-1}
Permeation channel inlet velocity	0.05 m s^{-1}
Inlet temperature	700 K
Reactive channel operating pressure	5 atm
Steam to fuel ratio	3
Air to fuel ratio	1.5

Fig. 5 – (a) Temperature (K) and (b) H$_2$ distribution (mole fraction) in the channel pair.

3.2. Outside the membrane

The simulation conditions are summarized in Table 1. The following are the analysis based on the model results.

The temperature distribution inside the channel pair is shown in Fig. 5a. It can be found that the ATR of methane can achieve a temperature as high as 1100 K at the catalytic-support layer. The temperature has a uniform distribution in the catalytic-support layer, as it has a high thermal conductivity. Temperature gradient occurs in both channels at y-axial direction, due to the flow convection. The products have temperatures around 1050 K, when they are collected at the outlet.

The H$_2$ distribution inside the channel pair is shown in Fig. 5b. Mole fractions of 0.36 and 0.1 are achieved by the H$_2$ rich gas collected at outlet of the permeation channel and reactive channel, respectively. In the microfluidic reformer using catalytic-support membrane, the H$_2$ yield is greater than 2, which is significantly better than conventional membrane reformers [2,21]. The system benefits from the design that the permeation and reaction occur at the same site, where the mass transfer resistance has been minimized.

3.3. Inside the membrane

This section presents the species distributions and reactions inside the catalytic porous support, and the mass transfer through the membrane and porous-clear flow interface.

Fig. 6 shows the CH$_4$ and H$_2$ distributions in the catalytic-support layer of the membrane. CH$_4$ is observed only near the interface of the porous and clear flows, and its mole fraction decreases sharply along the depth of the porous support (Fig. 6a). This is because the lower diffusivity inside the porous-support layer restrains the CH$_4$ supply from the bulk flow to the catalytic layer after it was depleted by the ATR reactions. Distribution of H$_2$ is found in Fig. 6b. The H$_2$ permeation process takes most of the H$_2$ produced by the ATR away from the catalytic layer to the permeation channel. However, H$_2$ accumulation region is still found in the middle depth of the catalytic-support layer where is relatively far away from both the membrane and porous-clear flow interface, due to the absence of sufficient removal force.

It is observed from Fig. 6 that both CH$_4$ and H$_2$ rich regions exist near the front and rear interface of the porous-clear flow region. It can be explained by the effects of convection flux in the catalytic-support layer. Due to the sudden change of the
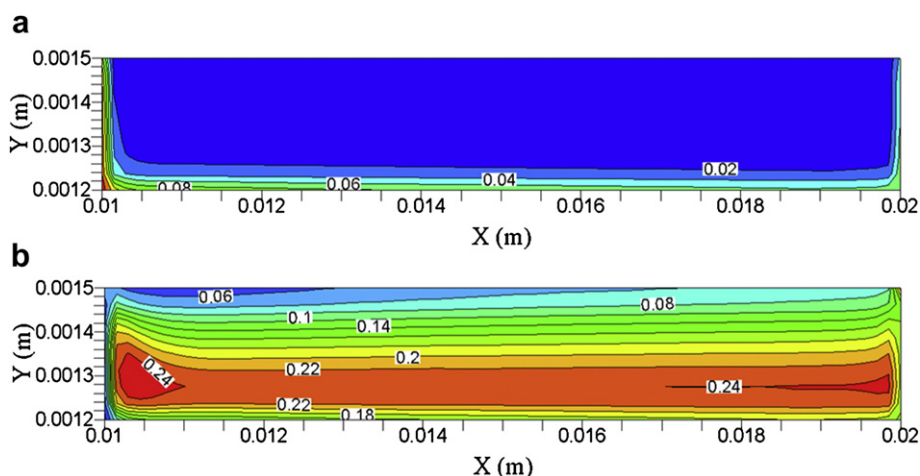

Fig. 6 – (a) CH$_4$ and (b) H$_2$ distribution (mole fraction) in the catalytic layer with H$_2$ permeation membrane.
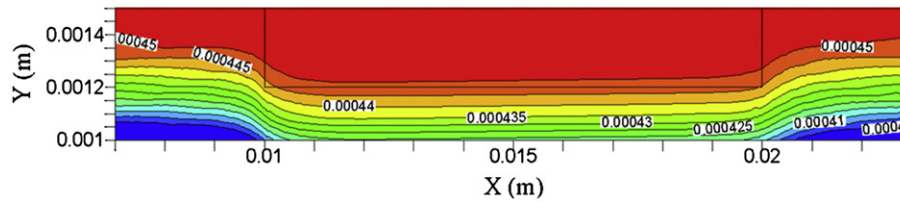
Fig. 7 – Stream function distribution (kg s⁻¹) near the interfacial region.

stream width, there forms convective flow to penetrate the porous layer at its front and rear interface, as shown in Fig. 7. This penetrative flow enhances the local mass transfer, and as a consequence, intensifies the local ATR rate. Therefore, the CH_4 can be retained and H_2 can be accumulated.

The same convective effect also affects the H_2 permeation rate. Fig. 8 shows the H_2 permeation rate along the membrane. The H_2-rich regions near the front and rear interface cause local higher H_2 flux through the membrane, due to the enhancement of local mass transfer and reaction rate by convective flow. At the remaining position, the H_2 flux slowly decreases along the membrane length, as more H_2 accumulates at the membrane surface in the permeation side (as depicted in Fig. 5b) that lowers the permeation driven force.

To investigate the interaction between the reaction and permeation, the effectiveness factors of four ATR sub-reactions (Eqs. (8)–(11)) are calculated based on the following equation and their calculated values are shown in Fig. 9:

$$\eta_i = \frac{\int_{0.0012}^{0.0015} \frac{R_i}{0.0003}dy}{R_i|_{y=0.0012}}. \tag{18}$$

Effectiveness factors of 0.125, 0.209, and 0.196 for R1, R2, and R4 can be read from the figure. Their increase at front and rear interface can also be attributed to the effect of mass transfer enhancement by convective flow, as explained in previous sections. Note that the effectiveness factor of R3 exceeds 1 and lies in the range between 2.59 and 6.21, which implies R3 (water-

gas shift) has a much higher reaction rate inside the porous layer than at the interface. Such phenomena have never been reported in conventional membrane reformers. It can be explained by the fact that the permeation of H_2 shifts the equilibrium tending to favor H_2 production. However, the removal of H_2 does not show equivalent enhancement effects to the other three reactions compared with R3, because these reactions are still restrained by the local CH_4 concentration (seen in Fig. 6a).

3.4. Effects of GHSV

In this section, the effects of gaseous hourly space velocity (GHSV) on the reforming performance are discussed. This effect implies the interaction between the internal and external mass transfer. The CH_4 conversion and membrane H_2 flux against GHSV (from 3600 h⁻¹ to 64,800 h⁻¹) are shown in Fig. 10. It can be found that the CH_4 conversion decreases while H_2 flux increases with the increasing GHSV. It is because when the GHSV is increased, the transport at the porous support is enhanced due to the increasing local mass flow rate. Thus, hydrogen production rate is increased and consequently, H_2 flux through the membrane is enhanced. However, at the same time, more absolute amount of CH_4 is supplied to the reformer with the increase in GHSV. The exceedingly high supply of CH_4 results in a reduction in its conversion rate. At GHSV of 3600 h⁻¹, the system can achieve near 100% CH_4 conversion, and the membrane H_2 flux of 3.85×10^{-2} mol s⁻¹ m². It also indicates that there is a critical GHSV that further increase will show insignificant effect on
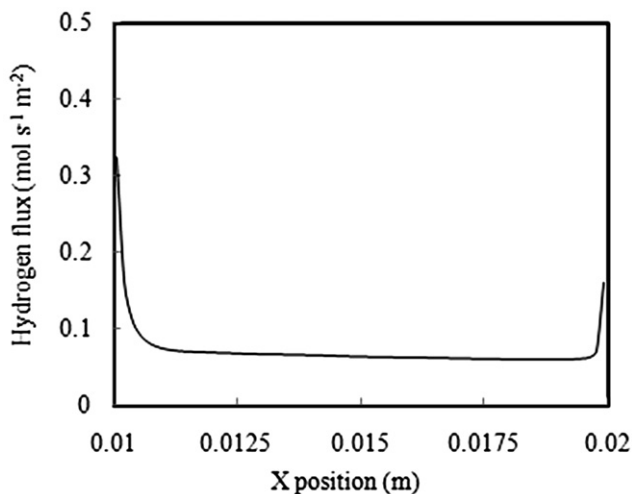

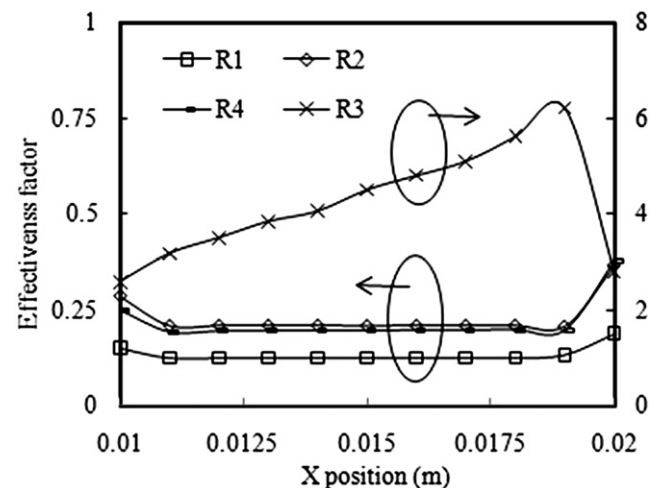**Fig. 8 – Hydrogen permeation flux through the membrane along x-axial direction.**

Fig. 9 – Effectiveness factors of ATR sub-reactions along x-axial direction.
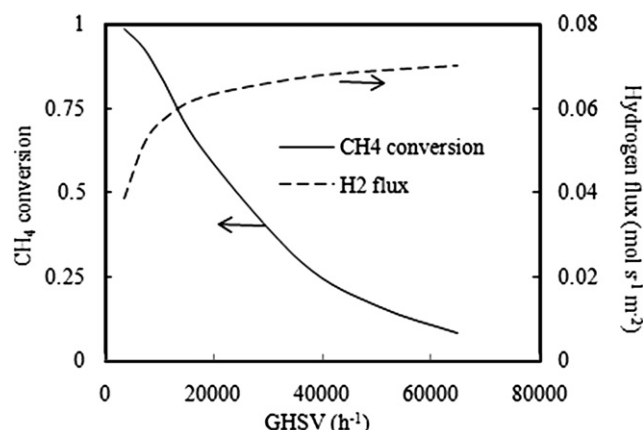
Fig. 10 – **Effect of GHSV on hydrogen flux through the membrane and methane conversion.**

improving the H_2 flux, while the CH_4 conversion will decrease quickly. Thus, any GHSV higher than the critical value is not remunerative during practical operation. Under the operating conditions given in this study, the critical GHSV is approximately 18,000 h^{-1}.

4.   Conclusions

This study investigated the chemical and transport characteristics of a novel microfluidic reformer with catalytic-support membrane for efficient hydrogen production and purification. A CFD model was developed and validated. The results revealed the relevant physicochemical phenomenon during the fuel processing. Exploiting the feature of catalytic-support membrane (i.e. instantaneous removal of H_2 at local reaction site), high membrane flux, H_2 yield, and fuel conversion are obtained under a short reactant residence time. It is noticeable that the water-gas shift reaction was intensified about 5 times, which is not possible in conventional membrane reformers. GHSV is also found playing important roles on the methane conversion and membrane H_2 flux. An optimal GHSV is suggested through parametric study. In general, the results provide useful implications to the applications of the catalytic-support membrane for building better micro-scale fuel processors.

Acknowledgment

REFERENCES

[1] Jensen KF. Microreaction engineering – is small better? Chem Eng Sci 2001;56:293–303.
[2] Xuan J, Leung MKH, Leung DYC, Ni M. A review of biomass derived fuel processors for fuel cell systems. Renew Sust Energy Rev 2009;13:1301–13.
[3] Sisworahardjo NS, Yalcinoz T, El-Sharkh MY, Alam MS. Neural network model of 100 W portable PEM fuel cell and experimental verification. Int J Hydrogen Energy 2010;35:9104–9.
[4] Agnolucci P. Economics and market prospects of portable fuel cells. Int J Hydrogen Energy 2007;32:4319–28.
[5] Peters TA, Stange M, Klette H, Bredesen R. High pressure performance of thin Pd-23%Ag/stainless steel composite membranes in water gas shift gas mixtures; influence of dilution, mass transfer and surface effects on the hydrogen flux. J Membr Sci 2008;316:119–27.
[6] Tsuru T, Morita T, Shintani H, Yoshioka T, Asaeda M. Membrane reactor performance of steam reforming of methane using hydrogen-permselective catalytic SiO_2 membranes. J Membr Sci 2008;316:53–62.
[7] Tsuru T, Shintani H, Yoshioka T, Asaeda M. A bimodal catalytic membrane having a hydrogen-permselective silica layer on a bimodal catalytic support: preparation and application to the steam reforming of methane. Appl Catal A Gen 2006;302:78–85.
[8] Nield DA, Bejan A. Convection in porous media. New York: Springer; 2006.
[9] Kumar A, Mazumder S. Assessment of various diffusion models for the prediction of heterogeneous combustion in monolith tubes. Comput Chem Eng 2008;32:1482–93.
[10] Ni M, Leung DYC, Leung MKH. Importance of pressure gradient in solid oxide fuel cell electrodes for modeling study. J Power Sources 2008;183:668–73.
[11] Fluent Inc. Fluent user's guide version 6.3. Lebanon: Fluent Inc.; 2003.
[12] Shi L, Bayless DJ, Prudich ME. A CFD model of autothermal reforming. Int J Hydrogen Energy 2009;34:7666–75.
[13] Hsueh C-Y, Chu H-S, Yan W-M, Chen C-H. Transport phenomena and performance of a plate methanol steam micro-reformer with serpentine flow field design. Appl Energy 2010;87:3137–437.
[14] Kim T. Micro methanol reformer combined with a catalytic combustor for a PEM fuel cell. Int J Hydrogen Energy 2009;34:6790–8.
[15] Duran JE, Mohseni M, Taghipour F. Modeling of annular reactors with surface reaction using computational fluid dynamics (CFD). Chem Eng Sci 2010;65:1201–11.
[16] Alkam MK, AL-Nimr MA. Improving the performance of double-pipe heat exchangers by using porous substrates. Int J Heat Mass Transfer 1999;42:3609–18.
[17] Xu J, Froment GF. Methane steam reforming, methanation and water-gas shift: I. Intrinsic kinetics. AIChE J 1989;35:88–96.
[18] Ma L, Trimm GF, Jiang C. The design and testing of an autothermal reactor for the conversion of light hydrocarbons to hydrogen I. The kinetics of the catalytic oxidation of light hydrocarbons. Appl Catal A Gen 1996;138:275–83.
[19] Chan SH, Hoang DL, Ding OL. Transient performance of an autothermal reformer – a 2-D modeling approach. Int J Heat Mass Transfer 2005;48:4205–14.
[20] Patel KS, Sunol AK. Modeling and simulation of methane steam reforming in a thermally coupled membrane reactor. Int J Hydrogen Energy 2007;32:2344–58.
[21] Park J, Lee S, Lim S, Bae J. Heat flux analysis of a cylindrical steam reformer by a modified Nusselt number. Int J Hydrogen Energy 2009;34:1828–34.
[22] Hupmeier J, Baune M, Thoing J. Interactions between reaction kinetics in ATR-reactors and transport mechanisms in functional ceramic membranes: a simulation approach. Chem Eng J 2008;142:225–38.
[23] Xuan J, Leung MKH, Leung DYC, Ni M. Integrating chemical kinetics with CFD modelling for autothermal reforming of biogas. Int J Hydrogen Energy 2009;34:9076–86.

[24] Wang H, Leung DYC, Leung MKH, Ni M. Modeling of parasitic hydrogen evolution effects in an aluminum—air cell. Energy Fuels 2010;24:3748—53.

[25] Coroneo M, Montante G, Giacinti Baschetti M, Paglianti A. CFD modelling of inorganic membrane modules for gas mixture separation. Chem Eng Sci 2009;64:1085—94.

[26] Ding OL, Chan SH. Autothermal reforming of methane gas — modelling and experimental validation. Int J Hydrogen Energy 2008;33:633—43.

[27] Yang L, Zhang Z, Yao B, Gao X. Hydrogen permeance and surface states of Pd—Ag/ceramic composite membranes. AIChE J 2006;52:2783—91.